Journal of the European Ceramic Society 44 (2024) 6597–6606

Contents lists available at ScienceDirect

Journal of the European Ceramic Society

journal homepage: www.elsevier.com/locate/jeurceramsoc

Effect of yttrium-doped grain boundary on sintering behavior and properties of transparent $ZnAl_2O_4$ ceramics

Pengyu Xu [a], Hao Wang [b,*], Bingtian Tu [b], Honggang Gu [c], Weimin Wang [b], Shiyuan Liu [c], Chengliang Ma [a], Zhengyi Fu [b]

[a] Henan Key Laboratory of High Temperature Functional Ceramics, School of Material Science and Engineering, Zhengzhou University, Zhengzhou 450052, China
[b] State Key Laboratory of Advanced Technology for Materials Synthesis and Processing, Wuhan University of Technology, Wuhan 430070, China
[c] State Key Laboratory of Digital Manufacturing Equipment and Technology, Huazhong University of Science and Technology, Wuhan 430074, China

ARTICLE INFO

Keywords:
$ZnAl_2O_4$
Transparent ceramic
Sintering behavior
Pore closure
Grain boundary structure
Hot isostatic pressing

ABSTRACT

Pore-closed $ZnAl_2O_4$ ceramic can hardly be pressureless sintered from conventional (>100 nm) powder, which restricts the fabrication of the transparent ceramic by capsule-free hot isostatic pressing technique. This work focused on the effect of yttrium-doping on the microstructural evolution in the sintering of a ~180-nm $ZnAl_2O_4$ powder. At a concentration of 300 or 600 ppm, the yttrium ions segregated along the grain boundaries and contributed to ordered nanostructures, which could suppress abnormal grain growth in both air sintering and hot isostatic pressing. The optimized Y-doped $ZnAl_2O_4$ transparent ceramic owned good visible light transmittance (>65 %) and a wide transmission range (6.0 μm at the 60 % transmittance) at a thickness of 1.5 mm, as well as high thermal conductivity (24.9 $W{\cdot}m^{-1}{\cdot}K^{-1}$) and reasonable mechanical properties (Vickers hardness of 12.9 GPa and Young's modulus of 281.3 GPa), meeting the application requirements for infrared windows.

1. Introduction

Transparent $ZnAl_2O_4$ ceramic (TZA) has attracted the attention of many researchers because of its unique and useful combination of the cubic lattice structure, wide transmission window, high thermal conductivity, interesting dielectric properties, and decent mechanical properties [1–6]. To fabricate TZA parts that meet the requirements of potential applications (infrared windows/domes, antennas, lenses, etc.) in terms of quality, size, and shape, it is necessary to choose a reasonable route based on the material characteristics.

Pressureless sintering (PS) is cost-effective and grants full freedom to the size and shape of the products [7]. Moreover, it can be conducted in air (i.e., air sintering, AS) [8,9] or even the oxygen atmosphere [10,11] to suppress the evaporation of MgO, ZnO, PbO, In_2O_3, etc. Unfortunately, mere PS has not yet offered sufficient densification for $ZnAl_2O_4$ ceramics to transparency. Spark plasma sintering (SPS) [3,4,12–14] and hot pressing (HP) [15–17] technologies can apply an external uniaxial pressure, which provides a significant contribution to the driving force for sintering, but have only produced small-size TZA samples (to the best of our knowledge, cylinders with a diameter of no more than 15 mm), and carry a risk of carbon contamination. The combination of PS and capsule-free hot isostatic pressing (HIP) technology has become the most common and reliable method for preparing high-quality transparent ceramics with high flexibility in size and shape [9,18–24]: HIP uniformly loads gas pressure and requires pre-PS to accomplish pore closure. Goldstein et al. [2] demonstrated that TZA can be accessed using an ultrafine powder (~12 nm) by AS combined with HIP. Nonetheless, some problems were exposed. For one thing, such nanoparticles have potential downsides. For instance, a stronger tendency to agglomerate may cause inhomogeneity of the green body and a challenge in adapting to colloidal forming technology to obtain complex-shaped samples [18,25]. However, the densification of conventional (>100 nm) $ZnAl_2O_4$ powder is inadequate to achieve zero apparent porosity through AS [1,2,26,27] (as revealed in Section 3.1); it is significant to overcome such difficulty. For another, the required HIP temperature was still too high (1550 °C), resulting in coarse grain size and residual stress [2]. Therefore, the sintering temperature needs to decrease further to suppress the volatilization of zinc and control the microstructure.

Introducing sintering additives is a feasible solution. Researchers have discussed the effects of sintering aids on the sintering behavior, microstructure, and properties of TZAs prepared by SPS/HP. Fu et al. [3]

* Corresponding author.
E-mail address: shswangh@whut.edu.cn (H. Wang).

https://doi.org/10.1016/j.jeurceramsoc.2024.04.026
Received 5 February 2024; Received in revised form 27 March 2024; Accepted 11 April 2024
Available online 12 April 2024

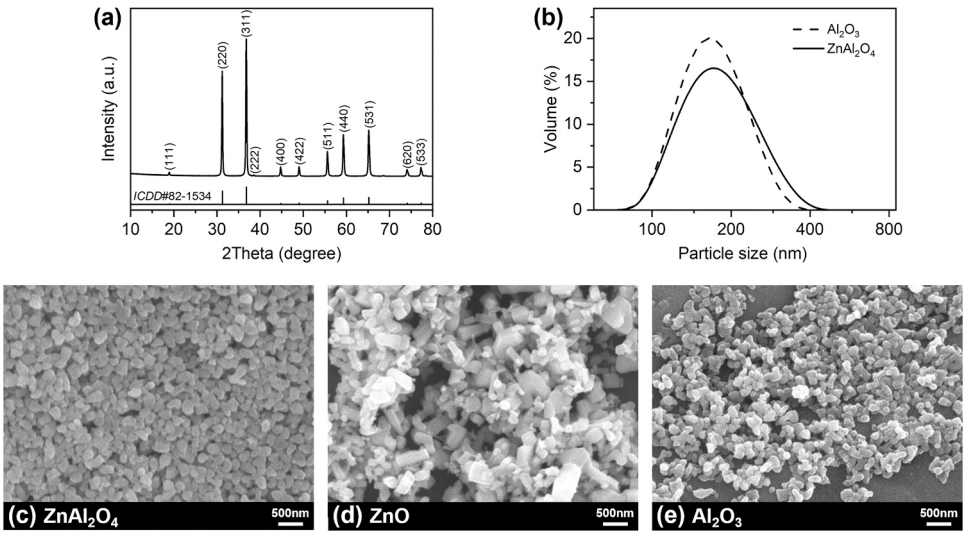

Fig. 1. Characteristics of the synthesized $ZnAl_2O_4$ powder. (a) XRD pattern. (b) Particle size distribution, the data of the Al_2O_3 raw powder is shown for comparison. (c) Morphology and (d–e) those of the reactants.

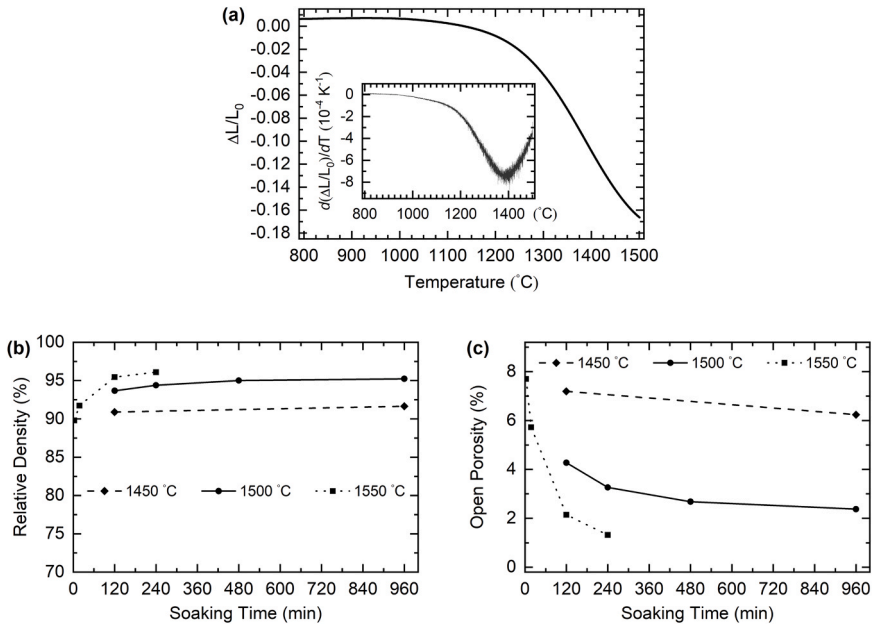

Fig. 2. Densification behavior of the undoped $ZnAl_2O_4$ green body upon AS. (a) Sintering shrinkage curve, inset shows the deduced shrinkage rate curve. (b) Relative density and (c) open porosity along soaking.

argued that SiO_2 transforms into a liquid state during heating, contributing to mass transport and reducing the sintering temperature. In addition, the liquid phase fills up part of the residual pores, which helps to minimize light scattering. Belyaev et al. [16] exploited the low melting point of ZnF_2 to promote particle rearrangement and matter transfer. Moreover, ZnF_2 has a high vapor pressure in the range of 800–1200 °C, which reduces its residue before closing of pores. Sokol et al. [14] found LiF not only a catalyst for the solid state reaction of ZnO and Al_2O_3 but also a promoter for both densification and grain growth. It is worth noting that silica and fluorides typically involve liquid-phase sintering mechanisms, which potentially trigger excessive grain growth. What is worse, they may remain in TZA as glassy intergranular phases and play the negative role of scattering or fracture sources [14].

Morz et al. [28] reported infrared-transparent $MgAl_2O_4$ ceramics with refined grains fabricated by pressureless sintering plus HIP and doping Y_2O_3. However, the author did not describe the experimental details, such as the particle size of the raw powder, the amount of dopant, and sintering conditions, nor did they analyze the role of Y_2O_3 in sintering. Moreover, Y_2O_3 proved an effective sintering aid for Al_2O_3 ceramic [29]. It functions by reducing the grain boundary migration rate at low temperatures, thus inhibiting both densification and grain coarsening at this stage [29]. Therefore, Y-doping may also be able to regulate the sintering behavior of $ZnAl_2O_4$.

This work aims to develop a feasible route for the production of TZAs suitable for application from conventional powder. Y_2O_3 was used as a sintering additive for preparing TZA from a powder with a particle size of ~180 nm by AS and post-HIP. We focused on its doping effect on the microstructural development in the sintering of $ZnAl_2O_4$ ceramics to explore the possible mechanism. Additionally, the microstructure and properties of the TZAs were studied.

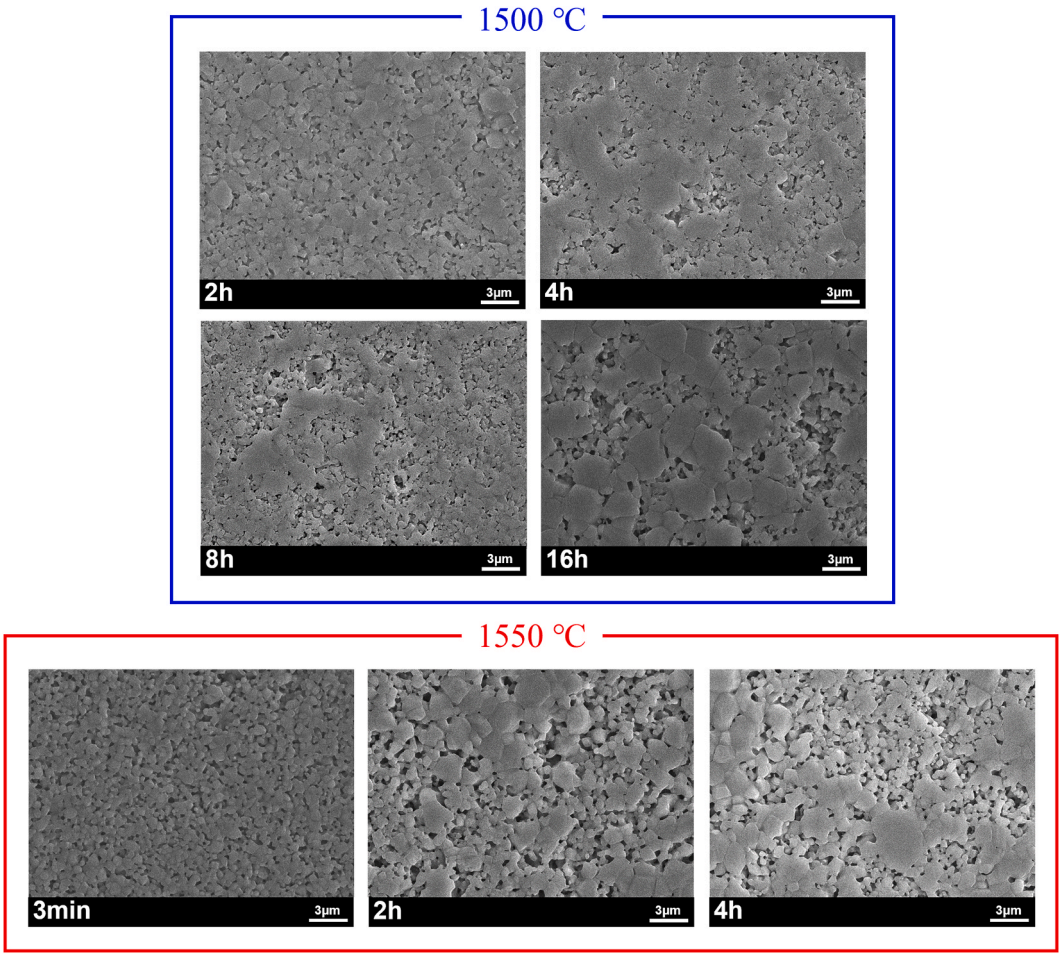

Fig. 3. Microstructure evolution of undoped $ZnAl_2O_4$ ceramic ASed at 1500 and 1550 °C.

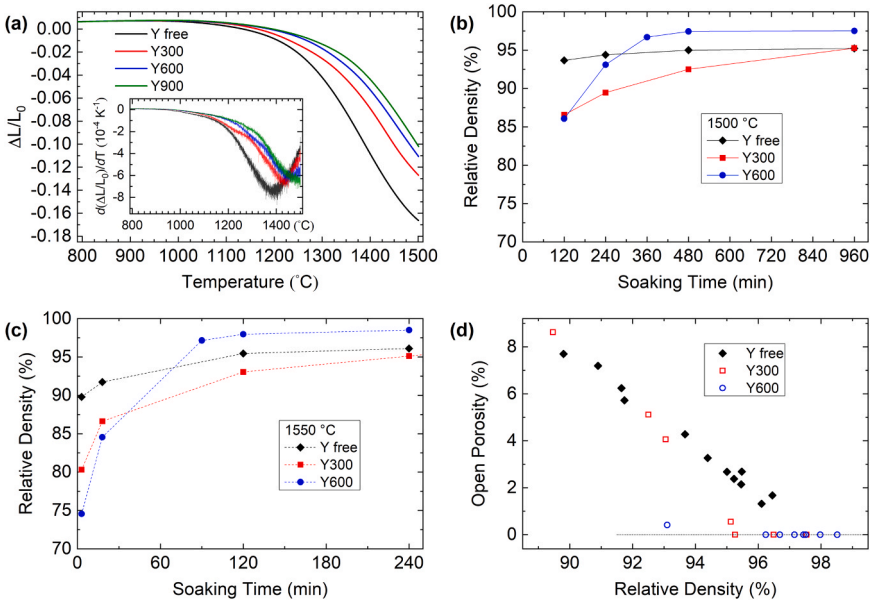

Fig. 4. Effect of Y-doping on the densification of $ZnAl_2O_4$ ceramics upon AS. (a) Sintering shrinkage curves, the deduced shrinkage rate curves are inseted. (b–c) Relative density along soaking. (d) Dependence of open porosity on relative density.

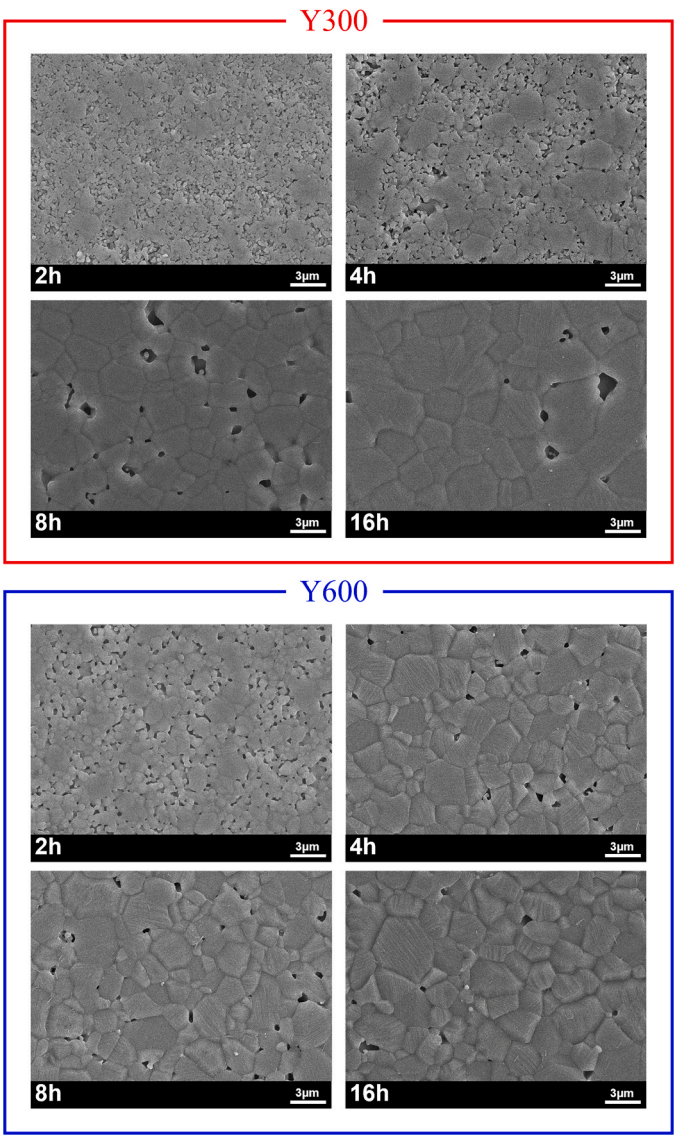

Fig. 5. Effect of Y-doping concentration on the microstructure evolution of $ZnAl_2O_4$ ceramic ASed at 1500 °C.

2. Experimental procedure

2.1. Processing

A $ZnAl_2O_4$ powder was synthesized by the solid-state reaction of commercially available ZnO and α-Al_2O_3, as described in our previous work [9]. High-purity alumina balls, an aqueous solution containing dispersants, plasticizers, and binders [9,30], and the $ZnAl_2O_4$ powder were combined in a polytetrafluoroethylene bottle. The mass of ceramic balls and total organic additives is 4 times and ~2.6 % of the powder mass, respectively. To dope yttrium with a concentration (relative to Al^{3+}) of 300, 600, or 900 ppm (hereafter referred to as Y300, Y600, and Y900, respectively), an aqueous solution of yttrium nitrate (4 N) with a concentration of 1 wt% was dropped into the mixture. After 10 h of ball milling, the slurry was freeze-dried and 50-mesh sieved to form soft granules. Subsequently, according to the designed sample size, the granules were weighed, uniaxial compacted with a 20- or 40-mm-diameter steel mold, and then cold isostatic pressed at 200 MPa for 5 min. In the next step, the green bodies were completely debonded by slowly heating to 800 °C in air[30]. Later, they were buried in dead-burned $ZnAl_2O_4$ powders and isothermally ASed in a $MoSi_2$ element electrical resistance furnace with a heating rate of 10 K/min, a sintering temperature of 1450–1550 °C, and a dwelling time of 3 min to 16 h. The post-HIP was performed at 1470 °C with a 180 MPa argon pressure for 5 h. Finally, the sintered samples were ground and polished on both surfaces.

2.2. Characterization

The crystalline phase was identified by X-ray diffraction (XRD, X'Pert Pro, Malvern Panalytical). The particle size distribution was characterized by a dynamic light scattering instrument (Zetasizer Nano ZS ZEN3600, Malvern Panalytical). The morphology of the powders and microstructure of the ceramics were observed by scanning electron microscopy (SEM, S-3400, Hitachi). The particle size of powders and ceramics with a low relative density (<85 %) was evaluated by averaging the diameter of at least 100 particles, while the average grain size of highly densified ceramics was estimated using the linear intercept method[31] by counting over 250 grains on the thermally-etched cross-sections. The length variation of the green body (40–1500 °C, 10 K/min) was recorded by a dilatometry (DIL402/NGB, Netzsch GmbH). The chemical composition of the TZA samples was analyzed with a full quantitative electron probe microanalyzer coupled with wavelength dispersive spectroscopy (EPMA-WDS, EPMA 8050 G, SHIMADAZU); the average results calculated from 10 areas are reported. A high-resolution transmission electron microscope (HRTEM, Talos F200S, FEI Quanta) and the attached energy disperse spectroscopy (EDS) were employed for a deeper insight into the microstructure, the samples were prepared by the focused ion beam (FIB) technique using a dual beam electron microscope (G3 UC Helios NanoLab, FEI Quanta). The density and open porosity were tested by the Archimedes method; for calculating the relative density, the theoretical density of $ZnAl_2O_4$ was taken as 4.606 g/cm^3 according to *ICSD*#75633 and the influence of trace Y_2O_3 doping was ignored. The optical transmittance was collected using spectrometers (UV-3550, Shimadzu, for 0.2–2.5 μm; 6700, Thermo Nicolet, for 2.5–25 μm). The refractive index in the wavelength range of 193−1690 nm was measured by a spectroscopic ellipsometer (ME-L, Wuhan Eoptics Technology) [32,33]; and from which derives the theoretical transmission limit [34]. The Vickers hardness was measured by a hardness tester (FALCON 400, INNOVA TEST) with a testing load of 0.1 kgf and a holding time of 15 sec. The elastic modulus was determined by an impulse excitation system (MK7, GrindoSonic). The thermal conductivity was measured at 25.0 °C using the laser flash method; the thermal diffusion coefficient and constant pressure heat capacity were acquired using a laser flash device (LFA457, Natzsch) and a differential scanning calorimeter (STA449c/3/G, Natzsch), respectively.

3. Results and discussion

3.1. Intrinsic air sintering behavior of $ZnAl_2O_4$ ceramic

3.1.1. Characteristics of the synthesized $ZnAl_2O_4$ powder

Fig. 1a gives the XRD pattern of the as-synthesized $ZnAl_2O_4$ powder, where a single gahnite phase was detected, signifying the complete reaction of ZnO and Al_2O_3. Both particle size distribution (Fig. 1b) and the SEM image (Fig. 1c) manifested that the particle size of the $ZnAl_2O_4$ powder is uniform, with an average of around 180 nm. By comparing the SEM photos of the product and reactants (Fig. 1c–e), it is noted that the $ZnAl_2O_4$ particles are similar to the Al_2O_3 raw ones in both size and morphology, which is attributed to the one-way migration of ZnO, instead of a normal counterdiffusion process, during the solid-state reaction between ZnO and Al_2O_3[35]. By utilizing this characteristic, $ZnAl_2O_4$ powder that shares a particle size distribution with commercial Al_2O_3 powder was accessed through a simple solid-state reaction route and is suitable for preparing transparent ceramics.

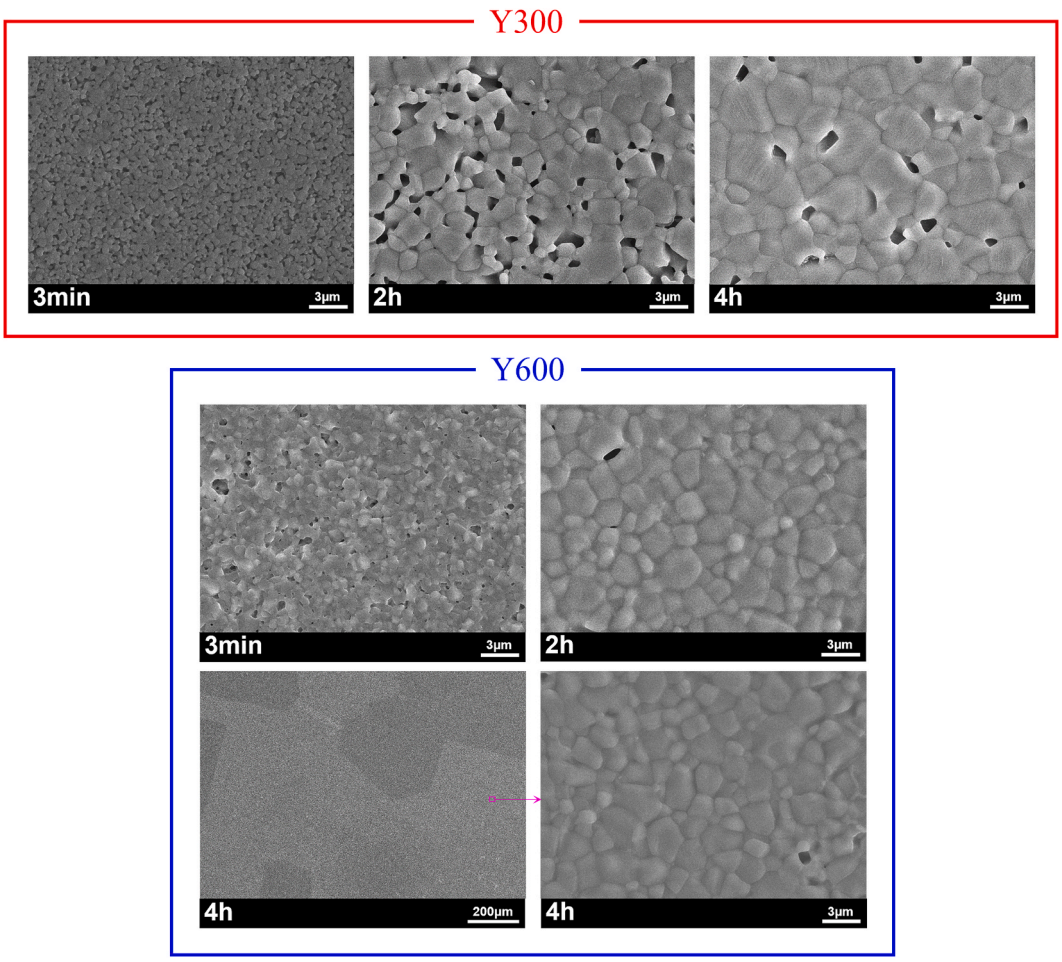

Fig. 6. Effect of Y-doping concentration on the microstructure evolution of $ZnAl_2O_4$ ceramic ASed at 1550 °C.

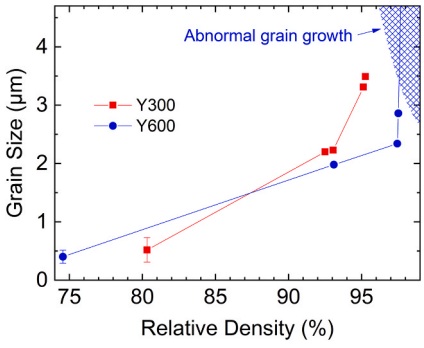

Fig. 7. Sintering path of the Y-doped $ZnAl_2O_4$ ceramics.

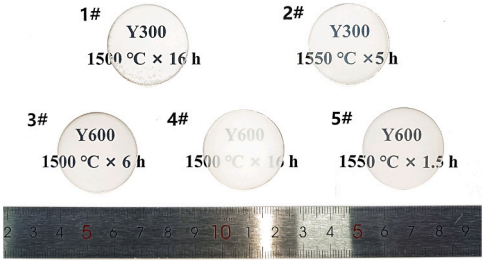

Fig. 8. Macrophotograph of TZA discs (ϕ 31 mm × 1.5 mm).

Table 1
Chemical compositions of transparent $ZnAl_2O_4$ ceramic samples, as determined by EPMA-WDS (wt%).

Sample number	ZnO	Al_2O_3
1#	44.18±0.21	55.82±0.21
2#	44.13±0.29	55.87±0.29
3#	44.19±0.23	55.81±0.23
4#	44.14±0.31	55.86±0.31
5#	44.20±0.28	55.80±0.28
Theoretical	44.387	55.613

3.1.2. *Densification behavior*

The thermal shrinkage curve of the undoped $ZnAl_2O_4$ green body is shown in Fig. 2a. The maximum shrinkage rate appears before 1400 °C, indicating good sintering activity. On this ground, isothermal sintering was conducted at 1450, 1500 and 1550 °C (a higher temperature may not be desirable due to the volatility of zinc) to observe the densification behavior. As shown in Fig. 2b, after holding at 1450 °C for 2 h, the relative density of the $ZnAl_2O_4$ sintered body had exceeded 90 %, which agrees with the shrinkage testing result. However, either extending the holding time or increasing the sintering temperature to 1500 or 1550 °C led to the increased relative density of the sample but failed to finish pore closure (Fig. 2c). Therefore, it was infeasible to eliminate residual pores by subsequent HIP. This result is similar to the previous AS studies of $ZnAl_2O_4$[1,2,26,27], where the pores cannot get completely closed after keeping at 1300–1700 °C for 2 h or longer.

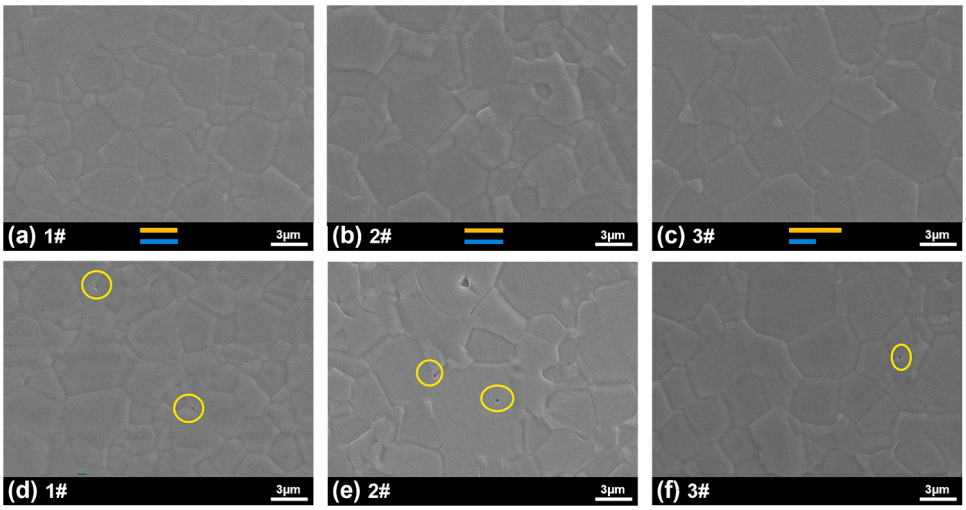

Fig. 9. SEM images of Samples 1#, 2# and 3#. (a–c) Typical microstructure, on which the lengths of orange and light blue bars denote their average grain size and those before HIP, respectively. (d–f) Pores are highlighted with ellipses.

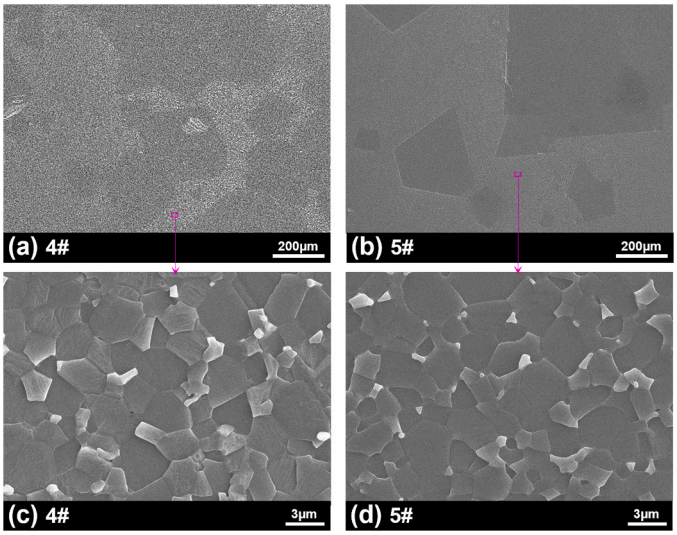

Fig. 10. SEM images of Samples 4# and 5#. (a–b) Full view. (c–d) Fine-grained region.

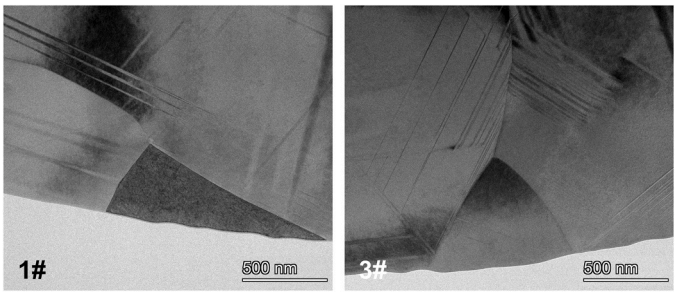

Fig. 11. TEM bright-field images of Samples 1# and 3# at low magnification showing high-density stacking faults.

3.1.3. *Microstructure evolution during air sintering*

Fig. 3 illustrates the microstructure evolution of $ZnAl_2O_4$ ceramics during isothermal sintering at 1500 and 1550 °C. After soaking for 2 h at 1500 °C or 3 min at 1550 °C, the grain growth was moderate since the open pore network in low-density samples effectively inhibited grain boundary migration. However, as sintering proceeded, such pore-pinning effect weakened as the density increased further, and thus, abnormal grain growth tended to occur [25,36]. The significant surface energy consumption of the powder by grain coarsening led to a lack of driving force for the follow-up densification. As a result, the closure of open pores in $ZnAl_2O_4$ ceramics can hardly be accomplished by continuous AS.

3.2. *Effect of Y-doping on the air sintering behavior of $ZnAl_2O_4$ ceramics*

3.2.1. *Densification under air sintering with constant heating rate*

In Fig. 4a, the sintering shrinkage curves of Y300, Y600, and Y900 green bodies are compared. Y-doping noticeably decreased the initial densification rate and raised the temperature to the peak of the densification rate. Below 1400 °C, the densification rate of the green body decreased with the increase of yttrium concentration. However, when the temperature rose to nearly 1500 °C, the densification rate of the green body with a higher yttrium concentration was even higher, indicating that a greater driving force for densification was reserved.

3.2.2. *Densification under isothermal air sintering*

According to the thermal shrinkage curve, the green bodies of Y300, Y600, and Y900 were isothermally ASed at 1500 and 1550 °C to investigate their sintering behavior further. Y900 was liable to differential sintering, which can be explained by the too-rapid and temperature-sensitive densification rate in the later stage. The changes in density during isothermal sintering of Y300 and Y600 are presented in Fig. 4b–c, which agrees with the results of thermal shrinkage testing. After a short dwell at 1500 or 1550 °C, a sample with a higher Y-doping concentration was less densified, implying that yttrium ions may play a similar role as in Al_2O_3 ceramic [29], namely, inhibiting diffusion in the early stage of sintering. As the soaking time extended, Y-doped samples could achieve higher density than the undoped sample. Another point worth noticing is that as the Y-doping concentration increased, the critical density (i.e., the density threshold for all open pores to get closed) decreased markedly, as shown in Fig. 4d, which was a positive factor for reaching pore closure earlier. Spusta et al. [37] studied the dependence of open and closed porosity on the relative density of Al_2O_3, $MgAl_2O_4$, and ZrO_2 ceramics during AS to conclude that the critical density is in large part a material characteristic and independent of the green body microstructure. This study demonstrates that a minute amount of sintering additive can also significantly affect the critical density.

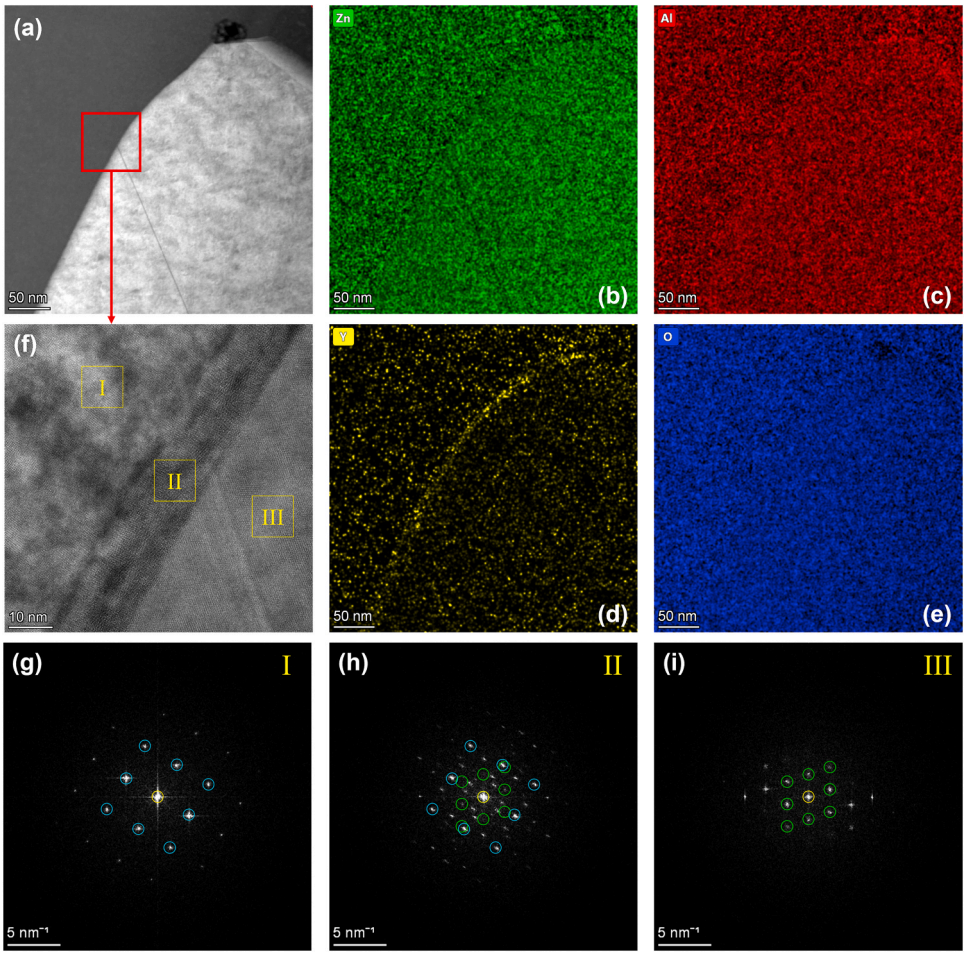

Fig. 12. TEM study of Samples 1#. (a) Scanning TEM–high-angle annular dark-field (STEM-HAADF) image and (c–e) elemental maps. (f) HRTEM image of the selected area marked in (a). (g–i) The FFT patterns of the selected areas in (f), where the diffraction points belonging to the $ZnAl_2O_4$ grains on both sides are marked by green and cyan circles, respectively.

3.2.3. *Microstructure evolution during isothermal air sintering*

The microstructure of Y300 and Y600 ceramics obtained by isothermal AS at 1500 and 1550 °C are shown in Figs. 5 and 6, respectively. Y300 and Y600 ceramics were free of abnormal grain growth at the complete closing of pores. Based on the measured density and statistics of grain size, the sintering path of Y300 and Y600 was outlined in Fig. 7. The trend line at low density was flatter with a higher Y-doping amount. That is to say, Y-doping retarded the grain growth that accompanied densification. Therefore, the surface energy consumption of $ZnAl_2O_4$ powder in the intermediate stage of sintering was reduced so that the green body maintained a high densification rate to complete the latest closure of pores without pore-grain boundary separation. This explains why Y-doping broke the relative density limit of ASed $ZnAl_2O_4$ ceramic. However, since pores in a sample with a high relative density tended to separate from the grain boundaries, sustained high-temperature sintering led to abnormal grain growth[36]. Fortunately, by doping yttrium, $ZnAl_2O_4$ ceramics with limited grain growth and isolated intergranular pores were prepared by AS, which were expected to be further densified via HIP at a lower temperature to fine-grained TZAs.

3.3. *Multiscale structure of transparent $ZnAl_2O_4$ ceramics and sintering behavior during HIP*

After HIP posttreatment, the Y-doped $ZnAl_2O_4$ ceramics with closed pores and free of abnormal grain growth became transparent, as exhibited in Fig. 8. The TZA samples are numbered 1# ~ 5#, and the underlying text indicates the doping concentration and AS conditions. The stoichiometry of $ZnAl_2O_4$ was maintained in all these specimens, according to the WDS data (Table 1). As illustrated in Fig. 9, under suitable sintering conditions (Samples 1#, 2# and 3#), both Y300 and Y600 ceramics obtained highly dense and homogeneous microstructure (Fig. 9a–c), with a few residual pores in some areas (Fig. 9d–f). According to the statistics of grain size (visualized as colored bars in Fig. 9a–c), additional grain growth was absent in Samples 1# and 2# upon HIP. That is to say, Y-doping with a concentration of 300 ppm froze microstructural coarsening in this period. By contrast, although the Y600 samples were of somewhat finer grains before HIP, the average grain size of Sample 3# was almost double after HIP, and Samples 4# and 5# even exhibited significant abnormal grain growth (Fig. 10), signifying the separation of the boundary from the pore upon HIP. The above results suggest that under the HIP condition in this study, the rate of grain boundary migration in a Y600 sample was higher than that in a Y300 one.

The microstructure of Samples 1# and 3# was explored in more detail using TEM. The high-density stacking faults (Fig. 11) suggest that plastic deformation was a contributing mechanism for densification during HIP [38,39]. In Sample 1#, triple-point pore with a very small size was detected (Fig. 12a). EDS mapping analysis (Fig. 12b–e) proves that the yttrium elements were concentrated at the grain boundaries even though the doping concentration was only 300 ppm. Although yttrium ions show a considerable solid solubility in $ZnAl_2O_4$ nanoparticles smaller than 10 nm [40], they could rarely substitute the Zn^{2+}/Al^{3+} at the lattice sites in the highly ordered crystalline grains

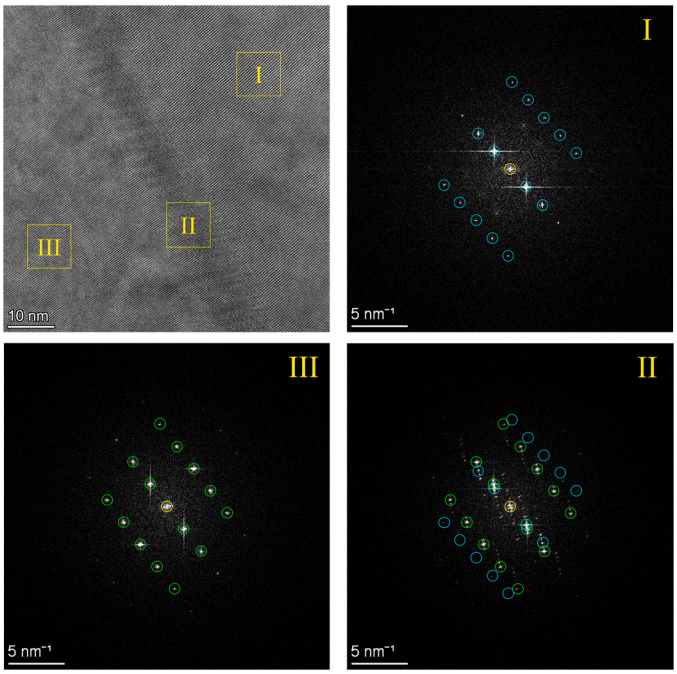

Fig. 13. HRTEM image near a grain boundary of Sample 3# and the corresponding selected-area FFT patterns, in which the diffraction points belonging to the $ZnAl_2O_4$ grains on both sides are marked by green and cyan circles, respectively.

because of the much larger radii [41]. HRTEM image (Fig. 12f) shows that the width of the "transition zone" (Region II) near the grain boundary is ~10 nm. By further analyzing the fast Fourier transform (FFT) patterns (Fig. 12g–i), it can be found that the diffraction signals of the grains on both sides overlap here, indicating that the interface between the two grains is not perpendicular to the observation direction, and the thickness of the grain boundary should be much smaller than the observed width. Apart from the diffraction signals belonging to the $ZnAl_2O_4$ grains, there were many additional diffraction spots with centrosymmetric distribution. A similar phenomenon was also observed in Sample 3# (see Fig. 13). The appearance of these spots indicates that the yttrium ions at grain boundaries were not disorderedly distributed, but rather contained within periodic structures.

Such Y-doped grain boundary nanostructures altered the mass transport properties during the sintering of $ZnAl_2O_4$ ceramics. Dillon et al. [42] revealed the direct correlation between the grain growth behavior and the grain boundary structure in Al_2O_3 ceramic: the grain boundary mobility is hindered by a sub-monolayer adsorbate whereas enhanced by the dopants segregation as double or multiple layers; such a relationship also works in other ceramics like Y_2O_3[43] and $MgAl_2O_4$[44–46]. According to the observed sintering behavior of Y300 and Y600 ceramics, the possible mechanisms can be speculated as follows. In the early stage of presintering, when the grain size was small, yttrium ions may not be enough to distribute throughout the grain boundaries, a higher concentration meant a larger occupation area of yttrium, and thus stronger suppression of grain boundary migration. A relevant clue was found by the comparison between the microstructure of the Y300 and Y600 ceramics before the complete closing of pores at 1500 °C (Fig. 5): the former was less homogeneous than the latter — which may be the reason why higher Y-doping concentration led to a lower critical density. The Y600 ceramics at critical density had finer microstructure than the Y300 ones, but their difference in grain size was not large, since Y-doping also reduced the densification rate at low temperatures (Fig. 4a). As grains grew during sintering, the surface area of grain boundaries gradually decreased. Accordingly, the grain boundaries had to adjust their structure to accommodate the yttrium ions. The grain boundaries in a Y600 sample were more prone to transform into a thicker type than those in a Y300 one with a larger but comparable grain size. In this way, the Y600 sample might overtake the Y300 one in the grain boundary mobility.

3.4. Properties of transparent $ZnAl_2O_4$ ceramics

Fig. 14a shows the ultraviolet-visible-near infrared transmittance of Samples 1# ~ 5#. The Rayleigh scattering caused by the Y-doped grain boundary nanostructures is estimated to be very weak since its dimension (see Figs. 12 and 13) was much smaller than the shortest

Table 2
Relationship between hardness and grain size of TZAs.

Number/ Reference	Grain size	Vickers hardness	Testing load	Note
1#	3.0 μm	12.9 ± 0.1 GPa	0.1 kgf	
2#	3.2 μm	12.9 ± 0.2 GPa	0.1 kgf	
3#	4.3 μm	12.5 ± 0.2 GPa	0.1 kgf	
4#	Abnormal	10.8 ± 0.3 GPa	0.1 kgf	
5#	Abnormal	11.0 ± 0.3 GPa	0.1 kgf	
[13]	10.1 nm	22.3 GPa	50 gf	
[13]	60.3 nm	18.3 GPa	50 gf	
[4]	0.54 μm	16.3 GPa	1 kgf	SiO_2
[2]	76 μm	10.5 GPa	0.3 kgf	residual stress
[14]	Abnormal	10.5 GPa	2 kgf	LiF

Table 3
Selected properties of TZA and comparison with those of $MgAl_2O_4$.

Properties	Value	$MgAl_2O_4$
Refractive index, n_D (λ = 589.3 nm)	1.7761	1.7150 [52]
Abbé number, V_D	51.2	60.5 [52]
Young's modulus (GPa)	281.3	277 [53]
Shear modulus (GPa)	109.5	110 [53]
Thermal conductivity ($W{\cdot}m^{-1}{\cdot}K^{-1}$)	24.9	~15 [51,53]

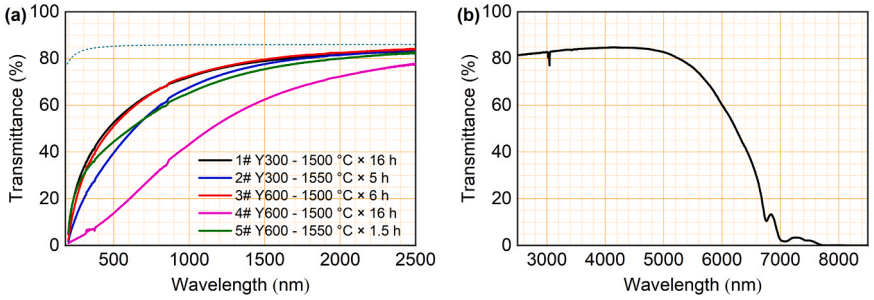

Fig. 14. Transmittance of the 1.5-mm-thick TZA discs. (a) Transmission spectra of Samples 1# ~ 5# in the ultraviolet-visible-near infrared region; the dashed line gives the theoretical limit calculated from the measured refractive index. (b) Mid-infrared transmission spectrum of Sample 1#.

wavelength in the transmittance measurement. The difference in transmittance from the theoretical value was mainly attributed to the scattering at the interface between residual pores (see Figs. 9, 10 and 12) and grains. The maximum visible transmittance of Samples 1# and 3# exceeds 65 %. In comparison, HIP at 1470 °C was less effective in eliminating residual pores on Samples 2# and 5# which were pre-fired at 1550 °C. The strategy that to obtain higher relative density at the end of presintering by lengthening the holding time improved the transparency of MgAlON and LiAlON ceramics [19,47]. However, in this work, Sample 4# lost the advantage in densification over the other samples HIPed at the critical density, due to the occurrence of abnormal grain growth.

The relationship between hardness and grain size of Samples 1# ~ 5# was investigated and compared with the results in the literature [2,4,13,14], as shown in Table 2. The hardness of TZA was noted to exhibit an evident Hall-Petch effect. In addition, the mechanical properties also depend on the Y-doped grain boundary nanostructures[48,49] and the high-density stacking faults in the grains [38,50]; a detailed visit on this theme is in progress.

Taking Sample 1# as a representative, the physical properties of TZA were evaluated. As shown in Fig. 14b, the spectral transmission window (transmittance exceeds 60 %) of the 1.5-mm-thick TZA extends to 6.0 μm, which is slightly larger than the value of a 1.0-mm-thick $MgAl_2O_4$. Considering that elevated temperature intensifies infrared absorption [51], TZA is expected to maintain better mid-infrared transmitting performance when it is thicker or operates at a higher temperature. From Table 3, it can be seen that the refractive index of $ZnAl_2O_4$ is higher than that of $MgAl_2O_4$ while the Abbé number is smaller [52], which coincides with the first-principles calculation [5]. The measured elastic moduli agree well with the theoretical value [6] and the experimental data of TZA obtained by SPS [12]; the Young's modulus is slightly higher than that of $MgAl_2O_4$. The thermal conductivity is as high as 24.9 $W{\cdot}m^{-1}{\cdot}K^{-1}$, much higher than that of $MgAl_2O_4$[51,53], which is consistent with the predicted results [1,6]. The above combination of properties endows TZAs with considerable competitiveness in the application of infrared windows.

4. Conclusions

In conclusion, yttria is an effective dopant that allows the fabrication of transparent $ZnAl_2O_4$ ceramics from a conventional powder by the combination of air sintering and capsule-free hot isostatic pressing. Yttrium ions were segregated between the $ZnAl_2O_4$ grains and participated in the construction of ordered grain boundary nanostructures, which altered the matter transport properties during sintering. With a Y-doping concentration of 300 or 600 ppm, abnormal grain growth could be prevented in both air sintering at 1500 °C and hot isostatic pressing at 1470 °C, thereby ensuring sufficient densification for pore closure and transparency, respectively. The thus prepared sample with a relatively large size (ϕ 31 mm × 1.5 mm) exhibited visible light transmittance higher than 65 % and a red edge of 6.0 μm for transmittance above 60 %, with a high thermal conductivity (24.9 $W{\cdot}m^{-1}{\cdot}K^{-1}$), and reasonable mechanical properties (Vickers hardness of 12.9 GPa and Young's modulus of 281.3 GPa), providing a good fit for the application requirements of infrared windows.

CRediT authorship contribution statement

Pengyu Xu: Conceptualization, Data curation, Formal analysis, Investigation, Methodology, Project administration, Software, Validation, Visualization, Writing – original draft, Writing – review & editing. **Hao Wang:** Conceptualization, Funding acquisition, Methodology, Project administration, Resources, Supervision, Validation, Writing – review & editing. **Bingtian Tu:** Funding acquisition, Project administration, Resources, Supervision, Validation, Writing – review & editing. **Zhengyi Fu:** Funding acquisition, Resources, Supervision. **Honggang Gu:** Data curation, Resources, Software, Visualization, Writing – original draft. **Weimin Wang:** Funding acquisition, Resources, Supervision. **Shiyuan Liu:** Resources, Supervision, Validation. **Chengliang Ma:** Funding acquisition, Project administration, Supervision.

Declaration of Competing Interest

The authors declare that they have no known competing financial interests or personal relationships that could have appeared to influence the work reported in this paper.

Acknowledgments

This work was supported by the National Key R&D Program of China (No. 2017YFB0310500), the National Natural Science Foundation of China (Nos. 51472195, 51502219 and 52272072), and the Collaborative Innovation Major Special Project of Zhengzhou (No. 20XTZX12025).

References

[1] N. Van der Laag, M. Snel, P. Magusin, G. De With, Structural, elastic, thermophysical and dielectric properties of zinc aluminate ($ZnAl_2O_4$), J. Eur. Ceram. Soc. 24 (8) (2004) 2417–2424.
[2] A. Goldstein, Y. Yeshurun, M. Vulfson, H. Kravits, Fabrication of transparent polycrystalline $ZnAl_2O_4$–a new optical bulk ceramic, J. Am. Ceram. Soc. 95 (3) (2012) 879–882.
[3] P. FuStudy of Preparation, Optical and Microwave Dielectric Properties of Spinel-Based Transparent Ceramics Huazhong University of Science and Technology (Ph. D. Thesis), 2014.
[4] P. Fu, Z. Wang, Z. Lin, Y. Liu, V.A. Roy, The microwave dielectric properties of transparent $ZnAl_2O_4$ ceramics fabricated by spark plasma sintering, J. Mater. Sci.: Mater. Electron. 28 (13) (2017) 9589–9595.
[5] P. Xu, H. Wang, L. Ren, B. Tu, W. Wang, Z. Fu, Theoretical study on composition-dependent properties of ZnO·$n$$Al_2O_3$ spinels. Part I: optical and dielectric, J. Am. Ceram. Soc. 104 (10) (2021) 5099–5109.
[6] P. Xu, H. Wang, L. Ren, B. Tu, W. Wang, Z. Fu, Theoretical study on composition-dependent properties of ZnO·$n$$Al_2O_3$ spinels. Part II: mechanical and thermophysical, J. Am. Ceram. Soc. 104 (12) (2021) 6455–6466.
[7] X. Liu, H. Wang, B. Tu, W. Wang, Z. Fu, Highly transparent $Mg_{0.27}Al_{2.58}O_{3.73}N_{0.27}$ ceramic prepared by pressureless sintering, J. Am. Ceram. Soc. 97 (1) (2014) 63–66.
[8] A. Goldstein, A. Goldenberg, Y. Yeshurun, M. Hefetz, Transparent $MgAl_2O_4$ spinel from a powder prepared by flame spray pyrolysis, J. Am. Ceram. Soc. 91 (12) (2010) 4141–4144.
[9] P. Xu, H. Wang, K. Zheng, B. Chen, M. Yang, Q. Chen, B. Wang, B. Tu, W. Wang, Z. Fu, Novel transparent ZnO·$3Al_2O_3$ ceramics prepared by reactive hot isostatic pressing, J. Eur. Ceram. Soc. 42 (2) (2022) 724–728.
[10] G.S. SNOW, Improvements in atmosphere sintering of transparent PLZT ceramics, J. Am. Ceram. Soc. 56 (9) (1973) 479–480.
[11] X. Wang, B. Lu, Influences of silica additive on sintering and Hall effect of novel transparent In_2O_3 semiconductive ceramics, Scr. Mater. 193 (2021) 137–141.
[12] B.-N. Kim, K. Hiraga, A. Jeong, C. Hu, T.S. Suzuki, J.-D. Yun, Y. Sakka, Transparent $ZnAl_2O_4$ ceramics fabricated by spark plasma sintering, J. Ceram. Soc. Jpn. 122 (1429) (2014) 784–787.
[13] C. Yang, A. Thron, R. Castro, Grain boundary strengthening in nanocrystalline zinc aluminate, J. Am. Ceram. Soc. 102 (11) (2019) 6904–6912.
[14] M. Sokol, S. Meir, E. Strumza, S. Kalabukhov, S. Hayun, N. Frage, On the effects of LiF on the synthesis and reactive sintering of gahnite ($ZnAl_2O_4$), Ceram. Int. 43(17) (2017) 14891–14896.
[15] P. Loiko, A. Belyaev, O. Dymshits, I. Evdokimov, V. Vitkin, K. Volkova, M. Tsenter, A. Volokitina, M. Baranov, E. Vilejshikova, Synthesis, characterization and absorption saturation of Co: $ZnAl_2O_4$ (gahnite) transparent ceramic and glass-ceramics: a comparative study, J. Alloy. Compd. 725 (2017) 998–1005.
[16] A.V. Belyaev, I.I. Evdokimov, V.V. Drobotenko, A.A. Sorokin, A new approach to producing transparent $ZnAl_2O_4$ ceramics, J. Eur. Ceram. Soc. 37 (7) (2017) 2747–2751.
[17] A.V. Belyaev, M.I. Lelet, N.I. Kirillova, N.M. Khamaletdinova, M.S. Boldin, A. A. Murashov, S.S. Balabanov, Sol-gel synthesis and characterization of $ZnAl_2O_4$ powders for transparent ceramics, Ceram. Int. 45 (4) (2019) 4835–4839.
[18] A. Krell, T. Hutzler, J. Klimke, A. Potthoff, Fine-grained transparent spinel windows by the processing of different powders, J. Am. Ceram. Soc. 93 (9) (2010) 2656–2666.
[19] R. Zhang, Y. Wang, T. Meng, H. Wang, Highly transparent LiAlON ceramic prepared by reaction sintering and post hot isostatic pressing, J. Eur. Ceram. Soc. 38 (15) (2018) 5252–5256.
[20] X. Zong, H. Wang, H. Gu, L. Ren, S. Guo, B. Tu, W. Wang, S. Liu, Z. Fu, Highly transparent $Mg_{0.27}Al_{2.58}O_{3.73}N_{0.27}$ ceramic fabricated by aqueous gelcasting, pressureless sintering, and post-HIP, J. Am. Ceram. Soc. 102 (11) (2019) 6507–6516.

[21] D. Yin, J. Wang, P. Liu, H. Zhu, B. Yao, Z. Dong, D. Tang, Fabrication and microstructural characterizations of lasing grade Nd:Y_2O_3 ceramics, J. Am. Ceram. Soc. 102 (12) (2019) 7462–7468.
[22] H. Wang, L.Y. Liu, P. Ye, Z. Huang, A.Y.R. Ng, Z. Du, Z. Dong, D. Tang, C.L. Gan, 3D printing of transparent spinel ceramics with transmittance approaching the theoretical limit, Adv. Mater. 33 (15) (2021) 2007072.
[23] P. Xu, H. Wang, W. Cui, Q. Chen, B. Tu, X. Sang, W. Wang, Z. Fu, ZnO·2.7Al_2O_3 nanocomposite with high optical transparency, J. Am. Ceram. Soc. 105 (6) (2022) 3735–3739.
[24] Z. Liu, J. Wei, G. Toci, A. Pirri, B. Patrizi, Y. Feng, T. Xie, D. Hreniak, M. Vannini, J. Li, Microstructure and laser emission of Yb:CaF_2 transparent ceramics fabricated by air pre-sintering and hot isostatic pressing, Opt. Mater. 129 (2022) 112540.
[25] M.N. Rahaman, Sintering of Ceramics, CRC Press, Boca Raton, 2007.
[26] C.W. Zheng, S.Y. Wu, X.M. Chen, K.X. Song, Modification of $MgAl_2O_4$ microwave dielectric ceramics by Zn substitution, J. Am. Ceram. Soc. 90 (5) (2007) 1483–1486.
[27] S. Takahashi, A. Kan, H. Ogawa, Microwave dielectric properties and cation distributions of $Zn_{1-3x}Al_{2+2x}O_4$ ceramics with defect structures, J. Eur. Ceram. Soc. 37 (9) (2017) 3059–3064.
[28] T. Mroz, L.M. Goldman, A.D. Gledhill, D. Li, N.P. Padture, Nanostructured, infrared-transparent magnesium-aluminate spinel with superior mechanical properties, Int. J. Appl. Ceram. Technol. 9 (1) (2012) 83–90.
[29] R. Voytovych, I. MacLaren, M.A. Gülgün, R.M. Cannon, M. Rühle, The effect of yttrium on densification and grain growth in α-alumina, Acta Mater. 50 (13) (2002) 3453–3463.
[30] A. Krell, J. Klimke, Effects of the homogeneity of particle coordination on solid-state sintering of transparent alumina, J. Am. Ceram. Soc. 89 (6) (2010) 1985–1992.
[31] M.I. Mendelson, Average grain size in polycrystalline ceramics, J. Am. Ceram. Soc. 52 (8) (2010) 443–446.
[32] S. Liu, X. Chen, C. Zhang, Development of a broadband Mueller matrix ellipsometer as a powerful tool for nanostructure metrology, Thin Solid Films 584 (15) () (2015) 176–185.
[33] H. Gu, X. Chen, H. Jiang, C. Zhang, S. Liu, Optimal broadband Mueller matrix ellipsometer using multi-waveplates with flexibly oriented axes, J. Opt. 18 (2) (2016) 025702.
[34] A. Krell, T. Hutzler, J. Klimke, Transmission physics and consequences for materials selection, manufacturing, and applications, J. Eur. Ceram. Soc. 29 (2) (2009) 207–221.
[35] D.L. Branson, Kinetics and mechanism of the reaction between zinc oxide and aluminum oxide, J. Am. Ceram. Soc. 48 (11) (1965) 591–595.
[36] S. Guo, H. Wang, P. Xu, B. Wang, Y. Xiong, B. Tu, W. Wang, Z. Fu, Effect of pretreated microstructure on subsequent sintering performance of $MgAl_2O_4$ ceramics, Ceram. Int. 45 (6) (2019) 7544–7551.
[37] T. Spusta, J. Svoboda, K. Maca, Study of pore closure during pressure-less sintering of advanced oxide ceramics, Acta Mater. 115 (2016) 347–353.
[38] H. Xu, W. Ji, W. Guo, Y. Li, J. Zou, W. Wang, Z. Fu, Enhanced mechanical properties and oxidation resistance of zirconium diboride ceramics via grain-refining and dislocation regulation, Adv. Sci. 9 (6) (2022) 2104532.
[39] H. Xu, Y. Li, J. Yang, R. Yang, H. Liu, J. Jiao, Microstructure evolution of ultra-fine grained HfC ceramics with high hardness sintered under ultrahigh pressure by plastic deformation densification mechanism, Int. J. Refract. Met. Hard Mater. 118 (2024) 106425.
[40] R. Samkaria, V. Sharma, Effect of Y^{3+} substitution on the structural, dielectric, and electrical properties of nanosized $ZnAl_2O_4$ spinel, Appl. Phys. A: Mater. Sci. Process. 115 (2) (2014) 697–704.
[41] R.D. Shannon, Revised effective ionic radii and systematic studies of interatomic distances in halides and chalcogenides, Acta Crystallogr Sect. A: Cryst. Phys., Diffr., Theor. Gen. Crystallogr. 32 (5) (1976) 751–767.
[42] J.D. Shen, M. Tang, W.C. Carter, M.P. Harmer, Complexion: a new concept for kinetic engineering in materials science, Acta Mater. 55 (18) (2007) 6208–6218.
[43] P.R. Cantwell, S. Ma, S.A. Bojarski, G.S. Rohrer, M.P. Harmer, Expanding time–temperature- transformation (TTT) diagrams to interfaces: a new approach for grain boundary engineering, Acta Mater. 106 (2016) 78–86.
[44] O. Schumacher, C.J. Marvel, M.N. Kelly, P.R. Cantwell, R.P. Vinci, J.M. Rickman, G.S. Rohrer, M.P. Harmer, Complexion time-temperature-transformation (TTT) diagrams: opportunities and challenges, Curr. Opin. Solid State Mater. Sci. 20 (5) (2016) 316–323.
[45] A.R. Krause, A. Kundu, O. Kosasang, R.P. Vinci, M.P. Harmer, The influence of grain boundary area on the complexion time-temperature-transformation diagram of Eu-doped magnesium aluminate spinel, Scr. Mater. 178 (2020) 251–255.
[46] C.J. Marvel, A.R. Krause, M.P. Harmer, Effect of Eu-doping and grain boundary plane on complexion transitions in $MgAl_2O_4$, J. Am. Ceram. Soc. 104 (8) (2021) 4203–4213.
[47] R. Zhang, H. Wang, T. Meng, Y. Wang, M. Liu, H. Wang, G. Zhang, Pressureless reaction sintering and hot isostatic pressing of transparent MgAlON ceramic with high strength, Ceram. Int. 44 (14) (2018) 17383–17390.
[48] L. Feng, R. Hao, J. Lambros, S.J. Dillon, The influence of dopants and complexion transitions on grain boundary fracture in alumina, Acta Mater. 142 (2018) 121–130.
[49] D.A. Rani, Y. Yoshizawa, K. Hirao, Y. Yamauchi, Effect of rare-earth dopants on mechanical properties of alumina, J. Am. Ceram. Soc. 87 (2) (2004) 289–292.
[50] X. Fang, Mechanical tailoring of dislocations in ceramics at room temperature: a perspective, J. Am. Ceram. Soc. 107 (3) (2024) 1425–1447.
[51] D.C. Harris, Materials for Infrared Windows and Domes: Properties and Performance, SPIE Optical Engineering Press, Bellingham, 1999.
[52] O. Medenbach, R. Shannon, Refractive indices and optical dispersion of 103 synthetic and mineral oxides and silicates measured by a small-prism technique, J. Opt. Soc. Am. B. 14 (12) (1997) 3299–3318.
[53] Technology Assessment & Transfer, Inc., Technical data – Transparent spinel ceramics. ⟨https://www.techassess.com/docs/f/pdf/Spinel-Properties-Data.pdf⟩, 2022 (accessed 20 June 2022).